Water- and Fat-Suppressed Proton Projection MRI (WASPI) of Rat Femur Bone

Yaotang Wu,[1,2,6*] Guangping Dai,[2,6] Jerome L. Ackerman,[1,2,5,6] Mirko I. Hrovat,[4] Melvin J. Glimcher,[1,6] Brian D. Snyder,[1,3,6] Ara Nazarian,[3,6] and David A. Chesler[2,6]

Investigators often study rats by μCT to investigate the pathogenesis and treatment of skeletal disorders in humans. However, μCT measurements provide information only on bone mineral content and not the solid matrix. CT scans are often carried out on cancellous bone, which contains a significant volume of marrow cells, stroma, water, and fat, and thus the apparent bone mineral density (BMD) does not reflect the mineral density within the matrix, where the mineral crystals are localized. Water- and fat-suppressed solid-state proton projection imaging (WASPI) was utilized in this study to image the solid matrix content (collagen, tightly bound water, and other immobile molecules) of rat femur specimens, and meet the challenges of small sample size and demanding submillimeter resolution. A method is introduced to recover the central region of *k*-space, which is always lost in the receiver dead time when free induction decays (FIDs) are acquired. With this approach, points near the *k*-space origin are sampled under a small number of radial projections at reduced gradient strength. The typical scan time for the current WASPI experiments was 2 hr. Proton solid-matrix images of rat femurs with 0.4-mm resolution and 12-mm field of view (FOV) were obtained. This method provides a noninvasive means of studying bone matrix in small animals. Magn Reson Med 57:554–567, 2007. © 2007 Wiley-Liss, Inc.

Key words: bone; MRI; WASPI; ultrashort T_2 imaging; solid-state MR imaging

Progress in developing new and improved methods for characterizing bone tissue has occurred at a rapid pace over the past decade, driven largely by the increasing importance of osteoporosis as a major public health concern in the elderly (1). A National Institutes of Health consensus development panel concluded in 2001 that in the United States alone, 10 million people had osteoporosis and 18 million more had low bone mass (2).

One of the crucial parameters that is used to determine bone quality is the degree of bone mineralization (also called the degree of mineralization, extent of mineralization, or sometimes simply "mineralization"), which is conventionally defined as the mass of bone mineral per volume of bone matrix. A closely related definition of the degree of mineralization is the ratio of bone mineral density (BMD) to bone matrix density. Knowledge of this parameter enables one to detect compositional changes in bone substance, and is a key asset for distinguishing osteoporosis (low BMD but normal mineralization) from other metabolic bone diseases, such as osteomalacia (low BMD and low mineralization) (3–6). Such data are also significantly useful for evaluating the effectiveness of treatment for heritable and metabolic diseases of the skeleton. The clinical significance of a diagnosis of mineralization defect in patients with low BMD is obvious, since appropriate measures can be undertaken to correct this abnormality in patients in whom the usual antiosteoporotic therapies would fail or might even be harmful. Indeed, defective mineralization is often discovered in patients undergoing bone biopsies to explain antiosteoporotic treatment failure (7). In the rapidly growing bones of children, some regions of normal active bone formation that have not yet reached full mineralization may be interpreted as osteopenic if only X-ray-based BMD information is available.

Methods to measure the calcium phosphate (Ca-P) mineral mass and characterize the individual chemical constituents of the Ca-P mineral crystals of bone tissue and bone substance have been developed to a high degree of sophistication (8). However, methods to quantify the content of bone matrix of intact specimens are lacking.

The clinical standard for characterizing bone mineral is dual-energy X-ray absorptiometry (DXA), in which a projective rectilinear scan of the bone at two X-ray wavelengths produces a 2D map of the bone mineral content. However, DXA BMD scores are dependent on the view direction, since DXA yields only a projective 2D image, and DXA BMD often fails to explain the reduction in fracture risk when therapeutic drugs are administered to treat osteoporosis (9). Although X-ray computed tomography (CT) can provide a true BMD in g cm^{-3} when a sufficient photon flux is used to ensure quantitative accuracy (i.e., quantitative CT (QCT)) and high spatial resolution, the radiation dose may be a consideration in frequent serial scanning of the torso, especially in children or women of child-bearing age. Additionally, no X-ray-based imaging modality can provide quantitative data on bone

[1]Laboratory for the Study of Skeletal Disorders and Rehabilitation, Department of Orthopaedic Surgery, Children's Hospital, Boston, Massachusetts, USA.

[2]Biomaterials Laboratory, Martinos Center, Department of Radiology, Massachusetts General Hospital, Charlestown, Massachusetts, USA.

[3]Orthopedic Biomechanics Laboratory, Department of Orthopaedic Surgery, Beth Israel Deaconess Medical Center, Boston, Massachusetts, USA.

[4]Mirtech, Inc., Brockton, Massachusetts, USA.

[5]Harvard-MIT Division of Health Sciences and Technology, Cambridge, Massachusetts, USA.

[6]Harvard Medical School, Boston, Massachusetts, USA.

Grant sponsor: National Institute of Biomedical Imaging and Bioengineering, NIH; Grant number: R01-EB004012; National Institute of Aging, NIH; Grant number: R01-AG014701; Division of Research Resources, NIH; Grant numbers: S10-RR16811; P41-RR14075; Grant sponsors: Peabody Foundation; MIND Institute; Athinoula A. Martinos Center for Biomedical Imaging.

*Correspondence to: Yaotang Wu, Laboratory for the Study of Skeletal Disorders and Rehabilitation, Department of Orthopaedic Surgery, Children's Hospital, 300 Longwood Ave., Boston, MA 02115. E-mail: yaotang.wu@childrens.harvard.edu

Received 12 May 2006; revised 20 November 2006; accepted 21 November 2006.

DOI 10.1002/mrm.21174
Published online in Wiley InterScience (www.interscience.wiley.com).

organic matrix content, which consists in large part of the solid fibrous structural protein collagen I.

Conventional (i.e., fluid-state) MR microimaging (MRμI) of bone images the marrow spaces of trabecular bone, which are filled with various proportions of hematopoietic (red) and fatty (yellow) marrow. Thus, MRμI produces a positive image of the interstitial spaces between trabeculae, which is equivalent to a negative image of the volume occupied by bone substance (mineral plus matrix). Such images reflect the effective porosity of the bone substance and provide a means to assess the gross geometry of cortical and trabecular bone, as well as a set of statistical microarchitectural descriptors of trabecular bone (10–12). However, because of the nature of this method, neither the BMD nor the matrix density can be obtained.

We previously demonstrated that bone mineral and matrix densities of relatively large porcine and bovine bone specimens can be obtained respectively by ^{31}P solid-state magnetic resonance imaging (^{31}P SMRI) and water- and fat-suppressed proton projection imaging (WASPI) (13–15). An in vivo ^{31}P SMRI study of human tibia has also been carried out (16). Other researchers, most notably Robson et al. (17) and Reichert et al. (18), have recently used ^{31}P and proton (^{1}H) MRI to image solid components of human bone. Glover and coworkers (19) utilized a 3D projection reconstruction technique to image boron-11 distributions. To allow excitation of short-T_2 resonances by a hard pulse in the absence of gradients, this method samples the signal during the ramp-up of the gradient following the excitation pulse. It is related to the methods we use (described below) to recover the central region of *k*-space lost during the receiver recovery time, and was recently used by Anumula et al. (20). Pauly and coworkers (21) previously developed short-T_2-selective sequences. Fernández-Seara et al. (22,23) used an adaptation of single point proton imaging to obtain images of bone, and studied matrix water content as a surrogate measure for the degree of bone mineralization. Mastikhin et al. (24) and Halse et al. (25) imaged the mineral content with a different adaptation of single-point imaging (single-point ramped imaging with T_1 enhancement (SPRITE)).

Rats are one of the most common animal models used by researchers to investigate the pathogenesis and treatment of skeletal disorders in humans. Rat bone specimens are widely studied by micro computed tomography (μCT), an X-ray based method (26–29) that essentially reflects only the mineral content of bone (i.e., the BMD) but not the solid matrix content.

In this study we explored the feasibility of WASPI for imaging the solid matrix content of rat whole bone specimens, and meeting the challenges of small sample size and demanding submillimeter resolution. The principles of WASPI are described in Ref. 15. In the current paper we emphasize the details of the solid-state MRI (SMRI) aspect of the method, particularly the recovery of critical data lost during the receiver dead time, which is essential for reliable quantitation.

The difference between SMRI and WASPI is that the SMRI method quantitatively collects *all* proton signals from both solid and fluid constituents. The WASPI method is built on SMRI, and includes a water- and fat-suppression preamble in the pulse sequence that is designed to achieve a good balance between reducing the fluid-state contributions to the image while minimizing the perturbation of the solid signal, to yield an image of only the solid or solid-like constituents.

MATERIALS AND METHODS

Materials

Four-month-old virgin female NIHRNU rats (Charles River Laboratories, Charlestown, MA, USA) were used in this study. The animals were euthanized via CO_2 inhalation prior to MRI. Following euthanasia the femurs were disarticulated from the hip and knee. The proximal and distal ends were stripped of soft tissue in order to expose the femoral head and neck and the distal femoral condyles. The remaining soft-tissue envelope was preserved. The specimens were wrapped in saline-soaked gauze until they were scanned by MRI and then by μCT. All procedures were authorized by and performed in accordance with the guidelines of the respective institutional animal care and use committees.

Carbon-black-filled styrene butadiene rubber (SBR) stoppers (size 13.5, top: 75 mm, bottom: 83 mm, length: 35 mm; Atlantic Rubber, Littleton, MA, USA) served as proton-containing phantoms for the organic matrix constituent of bone.

Two glass capillary tubes (outer diameter (OD): 1.5 mm, inner diameter (ID): 1.1 mm, wall thickness: 0.2 mm) were filled with normal saline to serve as a resolution test phantom.

Chicken bone marrow was extracted from chicken radii obtained from a local slaughterhouse and placed in glass tubes 2 or 4.6 mm in diameter. The chicken bone marrow (which has a high fat content) was used as a reference for water and fat suppression because the marrow in these rats is predominantly hematopoietic.

SMRI

Pulse Sequence

The basic SMRI pulse sequence consists of the following steps:

Step 1. A gradient pulse with all three gradient channels (G_x, G_y, and G_z) active is switched on. The magnitudes of the gradient vector **G** remain constant throughout all repetitions of the pulse sequence, and the gradient directions are naturally described in a spherical polar coordinate system and varied from one repetition to the next (Fig. 1). The use of gradients larger than the 10 mT/m strength used in routine clinical MRI enables us to recover desired spatial resolution in the face of an approximately several thousand Hz spectral linewidth due to the short T_2*. The rise time of the gradient is slow (1–3 ms). Safety issues with regard to nerve and muscle stimulation that may occur with temporal magnetic fields are not a concern in our case, since the slew rates of the gradient pulses are well below the FDA limits.

Step 2. A short, single, rectangular hard RF pulse is applied 1–3 ms after the gradient has reached its target value. The delay before the RF pulse permits the gradients to stabilize and any uncompensated fast eddy currents to

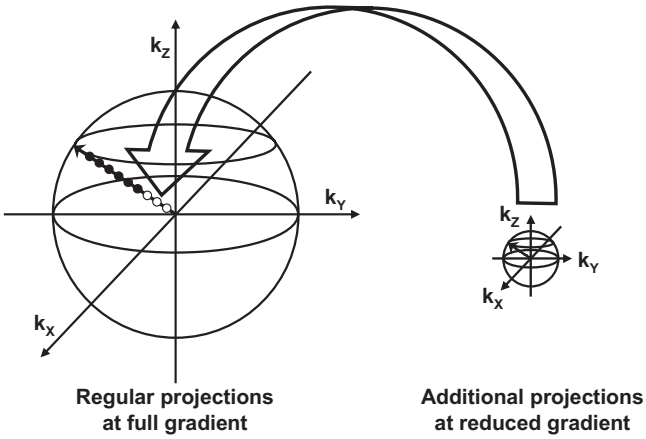

FIG. 1. *k*-Space trajectory of SMRI. Data samples in one repetition are acquired under a constant magnitude gradient vector, the direction of which varies from one repetition to the next. The solid circles represent acquirable points while the empty circles represent points lost in the receiver dead time. The arrow illustrates the scheme for recovering the lost data by performing an additional measurement under lower gradients and fewer gradient directions.

decay. The length of the RF pulse t_p (6–8 μs) is set to the Ernst optimum flip angle for maximal signal-to-noise ratio (SNR) at the chosen repetition time (TR). Since the pulse length is much shorter than the spin relaxation times of the interesting components of bone (solid mineral and matrix) and is well below 90°, the spin system can be approximated as a linear system. If the sinc function is taken to be zero beyond the first zero crossing on both sides, then the rectangular pulse at frequency ω_{rf} will excite nuclear spins resonating over a frequency range $|\omega - \omega_{rf}| < 2\pi/t_p$. More specifically, a short rectangular 8-μs pulse will excite nuclei resonating over a frequency bandwidth of about 250 kHz centered around ω_{rf} (30) (Fig. 2).

When dealing with solids, one must usually meet the criterion that B_1 dominates all other spin system interactions, including resonance offset and homonuclear direct dipolar spin-spin coupling, if it is to be fully effective. This is a much stronger requirement than that demanded by the linear system approximation. This criterion is clearly not satisfied in the present case, since the maximum resonance offset in the presence of the gradient field is much larger than $\omega_1 = \gamma B_1$ (e.g., $\omega_1/2\pi = 5.6$ kHz if 8 μs corresponds to a 16° pulse). One obvious result of the weak B_1, which impacts fluid and solid spin systems equally, is that a 180° pulse cannot be achieved at large resonance offsets. However, the criterion is met for on-resonance solid matrix components that have linewidths less than this bandwidth (T_2 as short as 57 μs). For voxels with large resonance offsets (at large distances from isocenter), the rotating frame effective field B_{eff} (resulting from the offset ΔB and applied RF B_1) is large and dominates the dipole–dipole interaction, further ensuring that the criterion is met for these solid matrix components—a phenomenon known as second averaging. Therefore, for the purposes of the solid-state imaging techniques used in this study (small flip angles, dipolar broadened linewidths no larger than ~5 kHz), all necessary requirements for the strength of B_1 are met.

Step 3. As soon as possible after the RF pulse is turned off (i.e., after the dead time (5–20 μs) of the receiver), the free induction decay (FID) is sampled. The sampling rate must be very fast (typically 2.5–10 μs per point, depending on the T_2 and the capability of the scanner), which enables us to acquire almost the full signal available from the subject. Except for signal loss during the receiver dead time, the rapidly decaying FID is acquired with high fidelity.

The many benefits of generating and sampling an echo, such as refocusing the unwanted defocusing caused by magnet inhomogeneity, chemical shift spread, and susceptibility distribution, as well as circumventing the receiver dead time problem, are outweighed by the almost complete loss of echo signal due to the very short T_2. Furthermore, attempting to adapt a conventional spin- or gradient-echo pulse sequence to the submillisecond T_2^* of bone matrix would require very short and intense RF pulses and huge, unsafe gradient ramp rates that violate FDA guidelines for peripheral nerve stimulation and exceed the capabilities of the scanner.

Likewise, it is important to note that if the slice-selection or self-refocusing RF pulses are on the order of 1 ms or longer in duration, they are ineffective for the solid constituents of bone tissue. The important criterion for slice selection or rephasing, namely that the magnetization isochromats follow specific trajectories under large flip angle pulses, is not the same as the small-flip-angle criterion in step 2. The solid-state magnetization is flipped by short, intense, small-flip-angle pulses even at large resonance offsets, but does not respond to long pulses in the same way fluid-state magnetization would (31) (e.g., some multiple quantum coherence might be generated, but no refocusing would occur).

Although there are similarities between our sequence and SPRITE (25), such as the excitation pulse applied during a fixed gradient and the acquisition of FIDs instead of echoes, there are significant differences. As its name implies, SPRITE is essentially a single-point imaging technique that achieves spatial resolution by pure phase encoding at a significant cost in SNR (most of the FID data are discarded), whereas our method achieves its spatial resolution by pure frequency encoding (at a cost of requiring

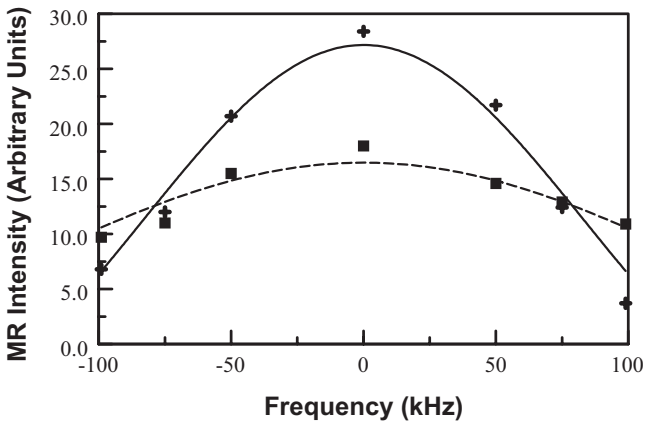

FIG. 2. Proton resonance frequency response to rectangular RF pulses. Crosses: Experimental MR signal of a small water phantom (ID = ~1.2 cm, height = ~0.6 cm) excited by an RF pulse of 8 μs (90° pulse = ~45 μs) with various frequency offsets. Solid line: Least-squares fit of the 8-μs pulse experiment with sinc(πx/125000). Squares: Experimental MR signal of the same water phantom excited by a pulse of 5 μs (90° pulse = ~45 μs). Broken line: Least-squares fit of the 5-μs pulse experiment with sinc(πx/200000).

gradients large enough to dominate spectral broadening). The multipoint SPRITE technique (25) acquires additional FID points to obtain T_2 data or to recover some of the lost SNR, but remains essentially a single-point method. The intended application of imaging live subjects (with the attendant requirement to keep long scan times as short as possible) demands that the higher-SNR method be used. Additionally, because preparation pulses are required for bone matrix imaging, the advantage of the 100% gradient duty cycle of basic SPRITE must be sacrificed.

Image Reconstruction

The image reconstruction is performed with the use of a particularly efficient method (32). The data points in a spherical polar coordinate system are first multiplied by $|\mathbf{k}^2|$ to compensate for the nonuniform density of the data in the **k** domain. A Hann (sometimes incorrectly denoted "Hanning") filter is next applied to the **k** domain data of each projection to reduce ringing artifacts at sharp edges in the image. The weighted and filtered polar data are blurred in *k*-space. It does not matter which blurring function is used, as long as the effect of the blurring function can be removed later. In the blurring function that we use, the *k*-space sample amplitude falls off linearly in each direction with a slope equal to the sample amplitude/grid size. The blurred data are then resampled onto a rectangular Cartesian coordinate system, followed by a 3D Fourier transformation. Finally, each point on the real space domain grid is multiplied by a function of distance from the real space origin to compensate for the effects of the blurring step (32). The size of the reconstruction grid is 64^3.

FOV and Spatial Resolution

The resolution limit of the projection imaging can be expressed as the projection pixel size (Δx_P), which one achieves by setting the FOV and the number of independent pixels (N_{IP}) across the FOV:

$$\Delta x_P = \mathrm{FOV}/N_{IP}. \quad [1]$$

FOV is determined by the size of the reconstruction matrix (M_{MAT}), the spectral width (W_S), the gradient amplitude (G), the magnetogyric ratio γ, and the number of samples per scan (N_{PS}):

$$\mathrm{FOV} = M_{MAT}W_S/(2\gamma G N_{PS}). \quad [2]$$

N_{IP} reflects the actual available linear spatial resolution as limited by the reconstruction, and is usually less than the number of discrete samples of the **k** domain data in each FID. N_{IP} is determined by the total number of projections (P), which we generate in a spherical polar coordinate system along a number N_R of equally spaced latitude rings:

$$P = (4N_R)^2/\pi, \quad [3]$$

$$N_{IP} = (P/\pi)^{1/2}. \quad [4]$$

Combining Eqs. [1], [2], and [4], we have

$$\Delta x_P = M_{MAT}W_S/\{(2\gamma G N_{PS})(P/\pi)^{1/2}\}. \quad [5]$$

If $M_{MAT} = 64$, $W_S = 200$ kHz, $G = 160$ mT/m, $N_{PS} = 80$, and $P = 2934$, then Δx_P is 0.4 mm, which is the protocol used in this study. Again, this represents the true pixel resolution as limited by the reconstruction.

The MR image resolution is also limited by the intrinsic pixel size (Δx_i), which is determined by the resonance line width (W_L) and the gradient strength applied during the imaging:

$$\Delta x_i \geq (2\pi W_L)/\gamma G. \quad [6]$$

Δx_i represents the limitation of the spatial resolution due to properties of the subject (specifically, the chemistry and physics of the bone tissue constituents). Assuming that the linewidth of the observed solid state proton signal is about 2 kHz, and the applied gradient is 160 mT/m, the resultant Δx_i is ~0.30 mm, and if W_L ~1.2 kHz, Δx_i ~0.16 mm. This means that in these two cases, the resolution of solid-state projection imaging is more limited by Δx_P and less by Δx_i.

Correcting Artifacts Caused by Missing Data Points in the Receiver Dead Time

The FID cannot be sampled closer to its origin than the extent of the receiver recovery time and probe ring down time (henceforth both of these terms are lumped together as "dead time" t_d) because the dissipation of the RF pulse power in the probe losses and the recovery of the overloaded preamplifier require a finite duration, which leads to erroneous initial data points. Another source of artifact is the phase dispersion that occurs during the RF pulse. Fortunately, the phase dispersion is quite linear across the usable receiver bandwidth. Thus the phase dispersion can be modeled as arising from an additional dead-time duration. The total dead time is then the acquisition delay due to the receiver dead time and probe ring down, plus some percentage of the RF pulse due to the phase dispersion. For a linear system where the sinc pulse approximation is valid, this percentage is theoretically 50%, but it can be as much as 60% for a 90° pulse. In the present study the RF pulse is very short, and the duration of half the pulse is less than a sampling dwell time t_{dw}; thus, only the $k = 0$ data point is lost during the RF pulse itself, and the missing data problem mainly arises from the dead time. The dead time is particularly severe in SMRI because T_2 is short, the sampling rate is fast, and creating an echo is not a practical option. These missing FID samples correspond to samples within $|\mathbf{k}_{lost}|$, the *k*-space close to the origin:

$$\mathbf{k}_{lost} = \gamma \mathbf{G} t_d. \quad [7]$$

Reconstructing an image from time-domain data with several points missed in the receiver dead time without any correction means that the time domain data are shifted in *k*-space, in a manner not equivalent to simply translating the time origin (which would be correctable in post-processing), but rather as data points that are moved radially toward the origin. This results in the Fourier trans-

form being multiplied by position-dependent phase factors. The magnitude of the phase shift varies linearly with k and is proportional to the amount of time shift (the dead time of the receiver). The intensity of the resulting image, which is a magnitude mapping of the Fourier transform of the time-domain data, would hence be seriously distorted by the various phase shift factors at different space positions.

Attempts to correct this problem by placing sampled data in the correct k-space positions and assigning zeros to the k-space positions of missing data are also not appropriate. The effect of setting the missing data to zero is equivalent to taking a convolution of the true image with a radial sinc function, which would depress the baseline of the image, resulting in a dark ring surrounding the image.

Many approaches to estimating the values of the missing points from the remainder of the data have been proposed (33). Our alternative approach is to measure them directly by means of a second acquired data set (34).

Let t_i be the supposed sampling times for the missing data, $i = 1, \ldots, i_{\text{lost}}$ (i_{lost} = the number of missing samples per projection):

$$\mathbf{k}(t_i) = \gamma \mathbf{G} t_i. \quad [8]$$

$$\mathbf{k}(t_i) < \mathbf{k}_{\text{lost}}. \quad [9]$$

Equation [8] shows that for the same value of k, if the amplitude of G is made smaller, then the sampling times t_i are replaced by longer ones. In other words, these missing samples can be approximated by a second set of projections with much smaller amplitude gradients $\mathbf{G}_1$ ($\mathbf{G}_1 \ll \mathbf{G}$). If $\mathbf{G}_1$ is small enough, it is possible that for acquirable sampling times t_j past the dead time, i.e., $t_j > t_{\text{d}}$:

$$\mathbf{k}_1(t_j) < \mathbf{k}_{\text{lost}}, \quad [10]$$

and

$$\mathbf{k}_{\text{sec}} = \gamma \mathbf{G}_1 t_{j\max} \sim \gamma \mathbf{G} t_{i\text{lost}}, \quad [11]$$

$$\mathbf{k}_{\text{sec}} \sim \mathbf{k}_{\text{lost}}, \quad [12]$$

where $\mathbf{k}_{\text{sec}}$ is the outermost position of this second data set in k-space. Equations [10] and [12] show that the data missed in the dead time of regular SMRI are recovered. This scheme is illustrated in Fig. 1.

In this project we used two different methods to acquire the second projection data with a reduced gradient. In one method, termed the DW-increased (dwell time-increased) method, the dwell time t_{dw} (i.e., the time between sampled complex data points) is increased by a factor C, so that the new dwell time Ct_{dw} is equal to the dead time ($Ct_{\text{dw}} = t_{j=1} = t_{i\text{lost}}$), while the gradient is reduced by that same factor C. In this method the Δk along a projection ray is the same for both the first and second acquisitions. In the second method, termed the DW-constant (dwell time-constant) method, t_{dw} is constant while the gradient is reduced by the factor of C. In this method the Δk along a projection ray is reduced by that factor of C in the second acquisitions. In other words, in the DW-constant method, some of the samples of this second data set are also lost in the dead time while the others are oversampled, and a subset of these are used to replace the missing data of the regular data set.

The sample exactly at the origin of k-space does not contribute to the reconstruction. The second set of data requires many fewer projections than the first set because the previously missing data do not extend far into k-space. The number of rings in k-space required in the second acquisition (N_{R2}) can be approximately determined by the number of rings used in the regular acquisition (N_{R1}) and the number of data points lost (N_{M}) per FID in a reconstruction matrix size of 64^3:

$$N_{\text{R2}} = N_{\text{R1}}(N_{\text{M}} - 1)/64. \quad [13]$$

For $N_{\text{M}} \leq 6$ and $N_{\text{R1}} \leq 24$, $N_{\text{R2}} = 2$ is sufficient. Except for the differences in gradient strength and the number of projections (P), all other pulse sequence and acquisition parameters are the same for both data sets.

Since the missing data are recovered at later times in the FID than they would be in the regular acquisition, a T_2* decay correction is applied in the second data set. Extending the maximum sampling time of the second data set $t_{j\max}$ substantially past T_2* would result in poor correction because such late time data would be measured with poor SNR. As long as $T_2{}^* > t_{j\max}$, this T_2* correction is minimal and in many cases may not be necessary.

In the reconstruction, the second data set is blurred and resampled onto the same rectangular Cartesian coordinate system of the first data set. It is treated in the same manner as the first set except for a weighting factor, which is the ratio of the number of projections in the first set to the second set, to compensate for the reduced number of projections. There is no requirement to have the projections of the second data set align in any particular way with the projections of the first data set. In the DW-constant method an additional weighting factor, which is the ratio of Δk in the first acquisition to that of the second acquisition, is applied to compensate for the increased sampling density along a projection ray.

WASPI

In addition to the short-T_2* problem that is common in imaging of solid materials, the presence of the dominant proton signal from fat and water in bone tissue is a major obstacle to the measurement of the true organic matrix density.

WASPI is a specially designed water- (WS) and fat-suppressed (FS) proton projection imaging pulse sequence that uses the large difference between the proton T_2*'s of the solid organic matrix and the fluid constituents of bone to suppress the fluid signals while preserving solid matrix signals, in contrast to conventional T_2-weighted imaging. The pulse sequence design is described in detail in Ref. 15.

The MRI experiments were carried out on a Bruker 4.7T 33-cm scanner equipped with a 400-mT/m gradient system (Bruker BioSpin, Billerica, MA, USA). The ^{1}H Larmor frequency was 200.13 MHz.

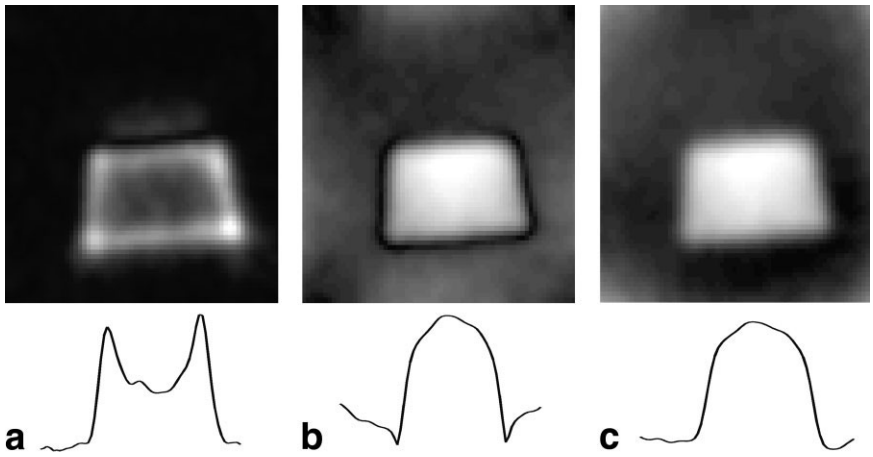

FIG. 3. ^{1}H SMRI of a rubber stopper. The sampling dwell time was 5 μs per complex point, and the receiver dead time was 10 μs. Two data samples of the FID were lost in the receiver dead time. **a:** Image reconstructed without correcting the data position in *k*-space, which resulted in severe distortion. **b:** Image reconstructed by zero-filling the missing data and assigning the acquired data to the correct *k*-space positions. Most of the artifacts were corrected, but a dark ring surrounds the image. **c:** Image reconstructed with additional data acquired under a 10-fold lower gradient magnitude. The artifacts were fully corrected.

SMRI data were acquired under the following protocol if not otherwise specified: The regular FID projection data were acquired under fixed 160-mT/m gradient magnitudes in 2934 directions at a sampling rate of 5 μs per complex point. The short, hard pulse used to excite the signal was 8 μs in duration, the receiver dead time was 10 μs, the TR was 0.15 s, and the FIDs were averaged over 16 acquisitions. The same MRI parameters were used in the second data set acquisition except that the number of projections (P) was 20 and the gradient magnitude was 80 mT/m with a sampling rate of 10 μs per complex point. The measurement time was approximately 2 hr, including both the regular and second sets of data acquisitions. Eighty complex points of the FID were used in the reconstruction, which effectively resulted in a 12-mm FOV in a 64 × 64 × 64 cubic lattice.

WASPI data were acquired with pairs of π/2 pulses (2–2.5 ms long) and π pulses (4–5 ms long), with frequencies set at the water and fat chemical shifts. The separation of these pulses was carefully arranged to reduce the possibility of water or fat echo formation. Other acquisition parameters for the WASPI experiments were the same as for the SMRI experiments.

Progressive saturation experiments were carried out to measure the T_1 of the solid bone matrix. Since T_2 is much shorter than the TR and its weighting effect on the signal can be neglected, the data were fitted to the following formula (35):

$$M = M_0(1 - \exp(-\mathrm{TR}/T_1))(\sin\beta) \div (1 - (\cos\beta)\exp(-\mathrm{TR}/T_1)), \quad [14]$$

where M_0 is the initial magnetization, and β is the excitation angle.

To obtain a better SNR in the small rat bone specimens and a uniform B_1 field over the FOV, we used a specially designed RF probe with a 15-mm-ID coil. To minimize dielectric losses in the sample, we employed a low-inductance distributed coil design (two turns with an equivalent capacitor C in series with each turn). Each turn consisted of a split 8-mm-wide copper strip with a 4-mm gap between the turns. The splits in the 8-mm-wide strips minimize eddy currents, and the gap produces a more homogeneous RF field across the FOV compared to an equivalent solenoidal coil. The unloaded Q for ^{1}H was 360.

To image the rubber stoppers, we used a relatively larger (ID = 15 cm) in-house-made birdcage coil.

Micro-CT (μCT) Experiments

μCT (μCT40; Scanco Medical AG, Bassersdorf, Switzerland) was utilized to image the bone mineral content of the intact rat bone specimens, and phantoms of dipotassium hydrogen phosphate (K_2HPO_4) were used to convert linear X-ray attenuation to equivalent bone mineral tissue density. The imaging parameters were as follows: 30 μm isotropic voxel size, 200 ms integration time (IT), 55 kV_p average beam energy, 0.145 mA beam current, and 1024 × 1024 image array size.

RESULTS

The importance of properly dealing with the receiver dead time and the missing data was demonstrated in ^{1}H SMRI scans of a rubber stopper and a rat bone femur.

In the experiment on the rubber, the regular projection data were acquired with W_S = 200 kHz, FOV = 15 cm, and P = 998. The excitation pulse was 12° (10 μs) and TR = 0.3 s. The receiver dead time was 10 μs, and the dwell time was 5 μs. Because of the receiver dead time, the first two data points in the *k*-space (not including the origin) were not acquired. The second set of projection data (with the weaker gradient) was acquired with the DW-constant method discussed above. All parameters in the second data acquisition were the same as those in the regular acquisition except for FOV = 150 cm, and P = 20.

Figure 3 shows the images reconstructed under three different schemes. Figure 3a shows the image reconstructed without any corrections, which resulted in severe distortions in the image. The intensities at the edge are much stronger than the intensity at the bulk of the stopper, although the true density of the stopper and the B_1 field of the birdcage coil are roughly uniform.

If the missing two points are set to zero and all the measured data are shifted two points toward the positive or negative *k*-space directions as appropriate (i.e., the measured data points are placed at the correct *k*-space posi-

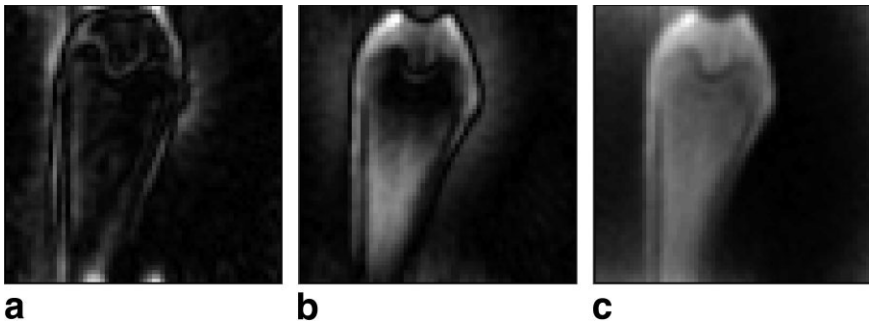

FIG. 4. ^{1}H SMRI of a rat femur specimen. The sampling dwell time was 5 μs per complex point, and the receiver dead time was 20 μs. Four points were lost in the receiver dead time. **a:** Image reconstructed without correcting the data position in the *k*-space, which resulted in severe distortion. **b:** Image reconstructed by zero-filling the missing points and assigning the acquired data to the correct *k*-space positions. Most of the artifacts were corrected, but a dark ring surrounds the image. **c:** Image reconstructed with additional data acquired under a fourfold lower gradient magnitude and dwell time of 20 μs. The artifacts were fully corrected.

tions without recovering the first two data points), the resultant image is largely corrected from the artifact shown in Fig. 3a. The intensity of the bulk of the rubber stopper is generally uniform, with a standard deviation (SD) of 6%; however, there are dark rings at the edge of the images of rubber stopper, which means that the baseline was depressed around the images (Fig. 3b). Finally, all of the artifacts were corrected (Fig. 3c) when the second projection data set was used in the reconstruction to compensate for the missing data.

In the SMRI experiment on a rat femur specimen shown in Fig. 4, the receiver dead time was 20 μs due to a longer ring-down of the RF power in the higher-*Q* coil. The number of missing data points was 4 with t_{dw} = 5 μs. The artifacts were more severe in the images reconstructed without the second projection data set (Fig. 4a and b). A second projection data set was acquired with the DW-increased method, i.e., the t_{dw} was increased from 5 μs in the first acquisition to 20 μs in the second acquisition, while the FOV was the same for both acquisitions at 12 mm. In the second acquisition, $P = 20$. We corrected the artifacts caused by missing data by including the second data set in the image reconstruction (Fig. 4c).

We expected a projection pixel size $\Delta x_p < 0.4$ mm for SMRI images achieved under the protocol W_S = 200 kHz (t_{dw} = 5 μs), P = 2934, G = 160 mT/m, and with the second projection data set acquired by the DW-increased method. This was demonstrated by imaging two closely spaced 1.5-mm-OD capillaries filled with normal saline (Fig. 5). The thickness of the capillary wall was 0.2 mm. The distance between the centers of the two capillaries was 1.5 mm and the total thickness of the adjacent walls of the capillaries was 0.4 mm. In both the longitudinal and axial directions there was a clear dark gap between the two saline tube images that corresponded to the adjacent walls of the capillaries. As discussed above, the spatial resolution in the SMRI images in this study was limited mainly by Δx_p.

We conducted SMRI and WASPI experiments on chicken bone marrow to adjust the water and fat suppression. Figure 6a shows the spectrum of freshly prepared bone marrow from chicken radii. The water and fat peaks are at 0.00 and –3.50 ppm respectively, in agreement with the data reported in the literature (36). Figure 6b shows the WS and FS spectrum of the same sample acquired with the WASPI sequence without the projection gradient, in

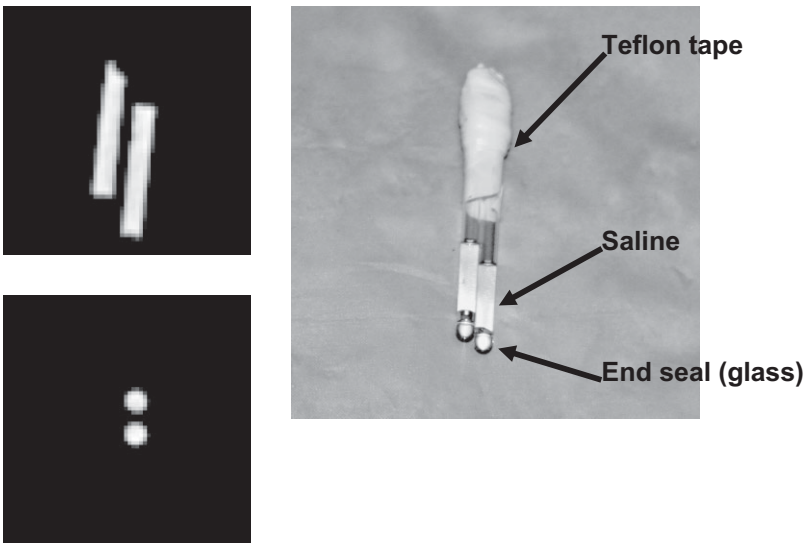

FIG. 5. ^{1}H SMRI of two capillaries filled with saline. The images were taken with number of projections P = 2934, FOV = 12 mm, G = 160 mT/m in a 4.7T scanner. OD of the capillary = ~1.5 mm, thickness of capillary wall = ~0.2 mm, separation between saline images = ~0.4 mm.

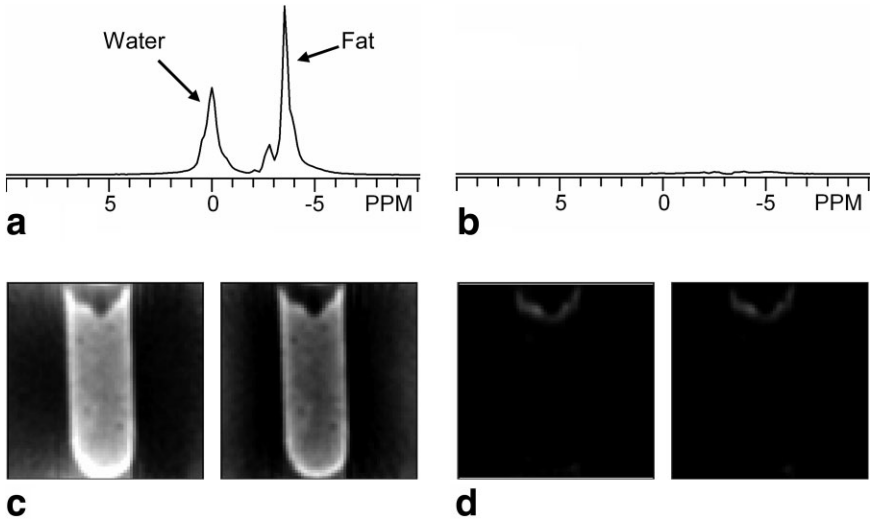

FIG. 6. Proton spectra, SMRI, and WASPI images of chicken bone marrow. **a:** Single-pulse proton spectrum of the sample. Water and fat peaks are at 0.00 and –3.50 ppm, respectively. **b:** WS and FS spectrum of the sample. The two peaks were reduced down to the baseline. **c:** SMRI of chicken bone marrow in a glass tube (ID = ~4.6 mm). Left: Image reconstructed with the second data set acquired by the DW-increased method. Right: Image reconstructed with the second data set acquired by the DW-constant method (shown on the same gray-scale level). **d:** WASPI of the same sample in c. Images were reconstructed with a second data set acquired by the DW-increased method (left) or the DW-constant method (right).

which the water and fat peaks were suppressed to the baseline. Figure 6c and d show the SMRI and WASPI images of chicken bone marrow in a 4.6-mm-ID glass tube. In the WASPI scan, the original 180° pulses (15) have been replaced by 90° pulses. The signal of bone marrow is suppressed in the WASPI images, except at the thin layer near the surface, where the air/marrow interface might distort the local field and cause failure of the frequency-selective suppression pulses. Quantitatively, the bone marrow signal in the WASPI image (Fig. 6d) is less than 4% of its SMRI signal (Fig. 6c). The FIDs were averaged by four scans. The SMRI and WASPI images were reconstructed with second data sets acquired by both the DW-increased and DW-constant methods; in cases both the gradients were reduced by a factor of 4. The general features of the images reconstructed with these two methods were identical, though the intensity of the image compensated by the DW-increased method was somewhat stronger.

Figure 7 shows the proton spectra of a rat femur bone specimen that contained only hematopoietic marrow. The single-pulse (8 μs) spectrum is featureless (Fig. 7a) except for the strong water resonance. The WS and FS spectrum, with the WS pulse frequency set at the peak of the resonance in Fig. 7a and the FS frequency at 3.50 ppm upfield, shows a broad resonance with reduced intensity (Fig. 7b), the full linewidth of which measured at half height was around 1.2 kHz (Fig. 7c). This resonance is considered to be mostly contributed from protons in solid bone matrix, either from water bound tightly to the matrix or from protons on collagen molecules (see Discussion section), since free water and fat signals were largely suppressed, as demonstrated in the above chicken bone marrow experiments. We eliminated other possible sources of proton signal inside and near the RF coil by using nonproton materials to construct the coil and sample-holder.

We carried out a series of progressive-saturation, 1D WASPI experiments on rat femur bone specimens to measure the T_1 of protons in the solid bone matrix. The WASPI parameters were the same as discussed above, except that the applied projection gradient was only in the *z*-direction to reduce the total experiment time. The *z*-gradient was applied to ensure that the observed signal was within the FOV and hence only from the bone matrix. The signal was averaged over 128 scans, and the TR was varied from 0.1 s to 5 s. The fitting results of the measured data to Eq. [14] showed that the proton T_1 of the rat bone matrix was ~3.7 s and the excitation angle was ~16° at 8 μs, corresponding to a 90° pulse of 45 μs (Fig. 8a). A measurement of the 90° pulse with a 4.6-mm-ID tube filled 8 mm high with water held at the center of the FOV showed the pulse length to be approximately 50 μs.

A rat femur specimen and a tube (ID = 2 mm) filled with freshly prepared chicken bone marrow (designated the "rat

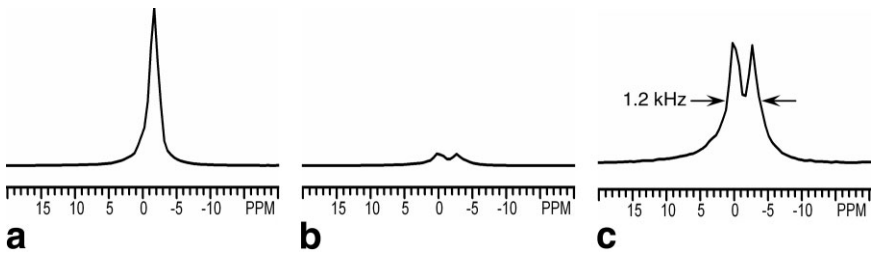

FIG. 7. Proton spectra of a rat femur bone specimen. **a:** NS one-pulse (8 μs) proton spectrum. **b:** WS and FS proton spectrum (shown in the same intensity scale as a). The suppression pulse frequencies were set at the peak at a and 3.50 ppm upfield, respectively. **c:** The vertical scale of b is enlarged 20-fold to display the linewidth, but the frequency scale is the same as that in a and b. The full width of the observed resonance at half height is ~1.2 kHz.

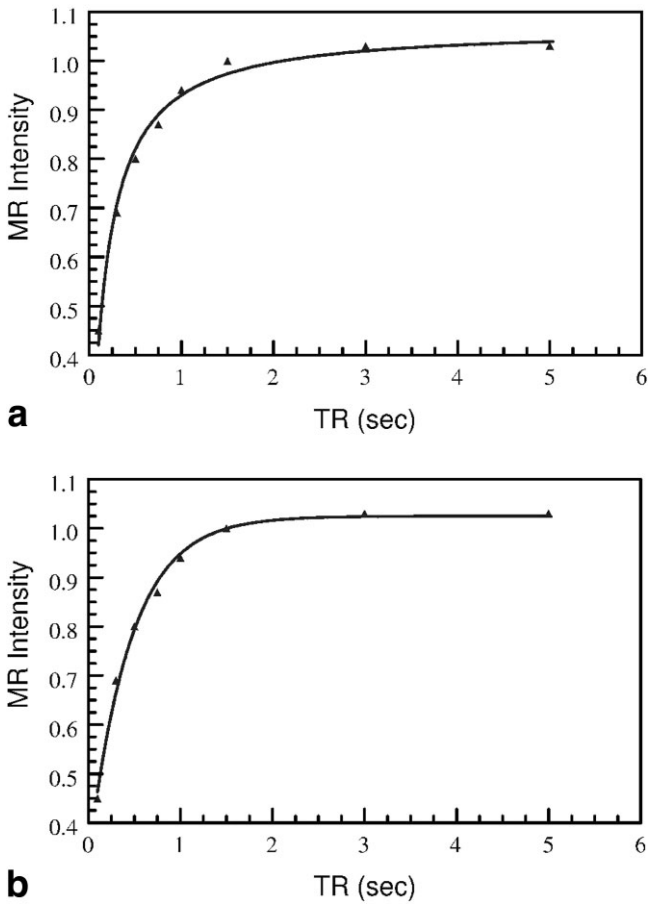

FIG. 8. Proton T_1 measurement of rat bone matrix. **a:** Data were acquired with a progressive-saturation sequence and fitted to Eq. [14], yielding T_1 = 3.7 s and excitation angle = 16°. **b:** T_1 curve-fitting with a standard three-parameter exponential formula. The fitting result showed a very short T_1 = 0.45 s, and B (in Eq. [16]) = 0.68. The meaning of B is ambiguous and cannot be reconciled with the exact expression except when the RF flip angle is near 90°. We recommend not using this model for small flip angles.

bone/chicken bone marrow sample") were mounted in a sample-holder (ID = ~13 mm) for spectroscopy and imaging studies. The proton single-pulse spectrum of this sample shows three peaks, which are assigned to bone water (0.00 ppm), chicken marrow water (–2.84 ppm), and chicken marrow fat (–6.34 ppm) (see below) (Fig. 9). The shift between the bone and chicken marrow water peaks is due to magnetic susceptibility and shimming effects.

SMRI and WASPI experiments were carried out on the rat bone/chicken bone marrow sample. Based on the above T_1 measurement, and taking a 16° excitation angle as the Ernst angle, we chose a TR of 0.15 s. Each projection signal was averaged over 16 scans, and the total measurement time, including the second data-set acquisition, was approximately 2 hr. Except for the WS and FS pulses in the WASPI experiments, all other parameters (i.e., projection numbers, FOV, gradient strength, and dwell times) were similar to those used for the SMRI and WASPI measurements on chicken bone marrow as described above. When three pairs of suppression pulses were utilized for WASPI, with frequencies set respectively at the three peaks shown in Fig. 9, all of the fluid-state signals were largely suppressed. The darker features in nonsuppressed (NS) SMRI images of the bone specimen (which indicate the location of the solid bone substance by exhibiting a lower detectable proton density than the marrow space) spatially matched the bright features in the WASPI images (Fig. 10). This observation clearly demonstrates that WASPI provides the solid-bone/matrix-only images of the sample.

When only one pair of suppression pulses, set at the frequency of 0.00 ppm (rat bone marrow water), was used, the resultant WASPI image (Fig. 11a) showed that the chicken marrow signal was not suppressed, but the marrow in rat bone was largely suppressed. This experiment clearly demonstrates that the 0.00-ppm peak was contributed from rat bone marrow, which in these rats was largely hematopoietic (watery) and relatively free of fat.

When two pairs of suppression pulses were set at the frequencies of –2.84 and –6.34 ppm, the resultant WASPI image (Fig. 11b) showed that the chicken marrow signal was basically suppressed, but the marrow in rat bone was not suppressed. This experiment demonstrates that these two peaks (–2.84 and –6.34 ppm) were contributed from the chicken marrow.

We conducted an experiment to determine whether the shift between the water peaks of rat bone and chicken marrow could be eliminated. Figure 12a shows the spectrum of the rat bone/chicken bone marrow sample after careful shimming. The two water peaks merged, and the fat peak was 3.50 ppm upfield from this peak. Figure 12b shows the WASPI images taken with two pairs of suppression pulses with frequencies at the two peaks shown in Fig. 12a. The signals of both the rat bone soft tissue and the chicken bone marrow are suppressed, leaving only the solid bone matrix.

μCT scans of the same rat femur bone specimen were taken using the parameters described in the Materials and Methods section. The resultant μCT images of 30 μm isotropic voxel size were coarsened to an isotropic voxel size of 150 μm to match the SMRI and WASPI images (Fig. 10). The bright areas of the μCT images arise from the mineral content of the bone substance, and should roughly match the WASPI image, which represents the matrix content of the bone substance. A reasonable geometrical correlation between μCT images and WASPI images is observed.

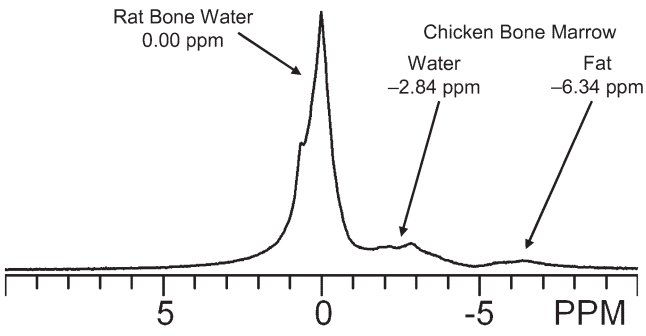

FIG. 9. Spectrum of a rat femur bone specimen and chicken bone marrow (one-pulse proton spectrum from a rat femur bone specimen and a tube of chicken bone marrow held in a sample-holder). The water peak resolved into two peaks that were ~2.84 ppm apart. The assignments of the peaks are described in the text.

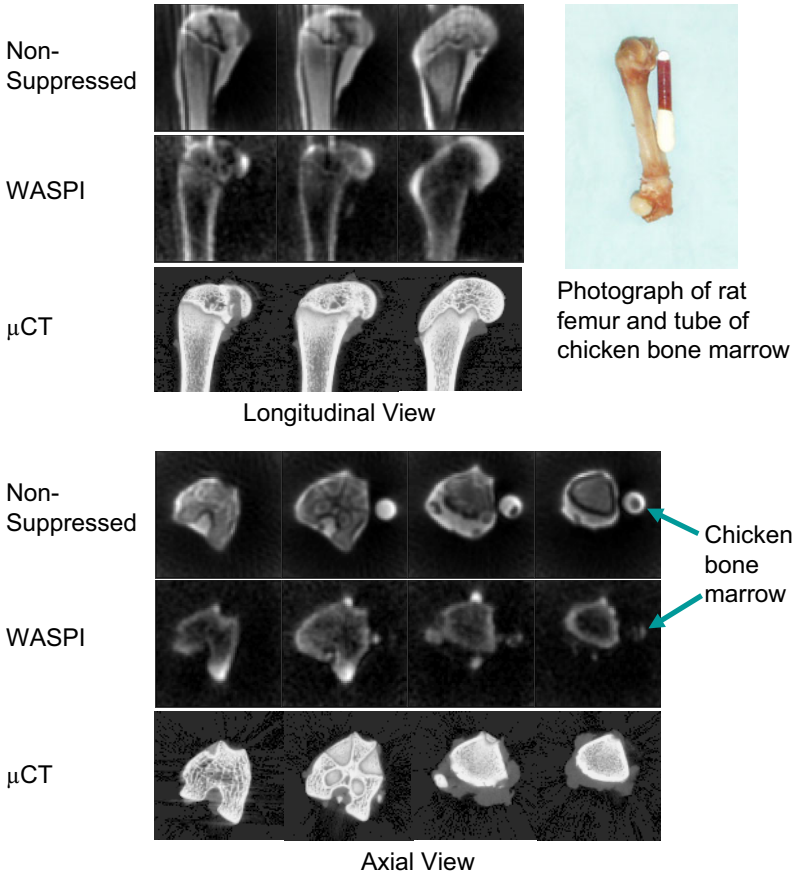

FIG. 10. NS, WASPI, and μCT images of a rat distal femur and a tube of chicken bone marrow held in a sample-holder. The bone substance is darker compared to the marrow spaces (due to proton-density differences) in the NS images, but is bright in the WASPI (suppression pulses at 0.00, –2.84, and –6.34 ppm) and μCT images.

DISCUSSION

We have demonstrated the efficacy of including a second data set acquired with the DW-increased or DW-constant method in the reconstruction to correct the artifacts caused by the missing data in *k*-space. However, reducing the gradient strength in the second data acquisition will compromise the intrinsic resolution. For example, in the DW-increased method, if the receiver dead time is 20 μs, one should increase the t_{dw} to 20 μs and reduce the W_S to 50 kHz, which will reduce the gradient applied during the second data acquisition by a factor of 4. According to Eq. [6], the intrinsic pixel size Δx_i of bone matrix with a resonance linewidth of 1.2 kHz will be four times larger than the Δx_i ~0.16 mm in the first data set acquired under the regular projection gradient strength. The overall resolution will be reduced. It is always better to use the shortest dead time that the scanner hardware and RF coil ringdown will allow. In this study, the dead time in the imaging of the bone specimens (Figs. 10–12) was set to 10 μs, and the gradient was reduced by a factor of 2. The corresponding Δx_i was ~0.34 mm, which is still less than the projection pixel size Δx_p of 0.4 mm. Thus, it is reasonable

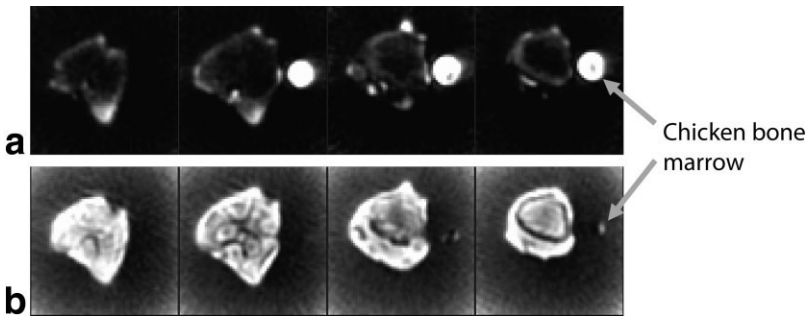

FIG. 11. WASPI of rat femur and chicken bone marrow with suppression pulses at various frequencies (shown on the same grayscale level). Four successive image slices are shown. **a:** One pair of suppression pulses with frequency at 0.00 ppm. The soft-tissue signal of the rat femur was suppressed but the signal of chicken bone marrow was not. This peak was assigned to rat bone water. **b:** Two pairs of suppression pulses with frequencies at –2.84 and –6.34 ppm. The signal of chicken bone marrow was suppressed while the soft tissue of rat femur was not. These two peaks were assigned to water and fat peaks of chicken bone marrow, respectively.

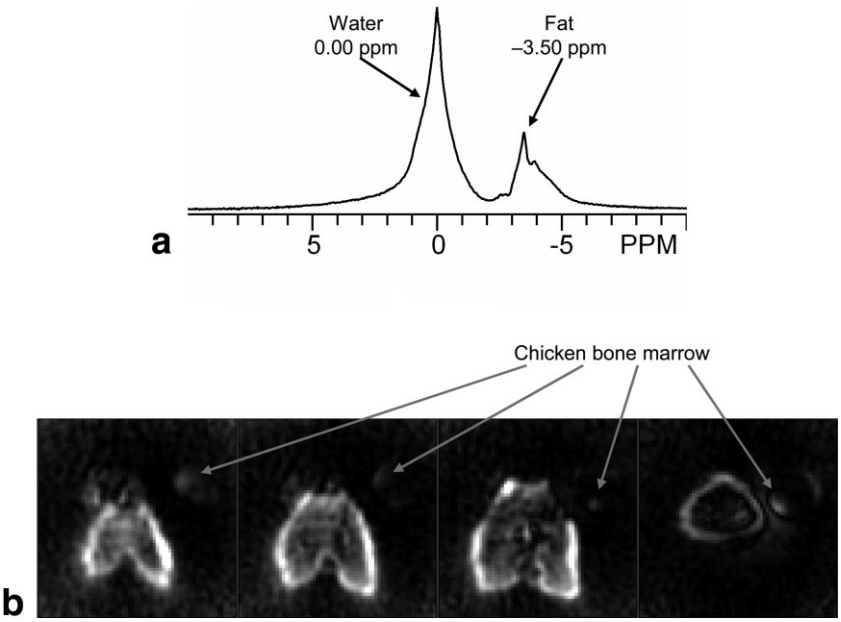

FIG. 12. Spectrum and WASPI images of a rat femur bone specimen and chicken bone marrow with better shimming. **a:** After careful shimming, the shift between water peaks of rat bone and chicken bone marrow was eliminated. **b:** WASPI images were taken with two pairs of suppression pulses with frequencies at the two peaks shown in a. The signals of chicken bone marrow and rat bone marrow were both suppressed, leaving only the bone matrix.

to assume that the spatial resolution of the bone matrix constituents is about 0.4 mm. Since the reconstruction contains data obtained at two different effective spatial resolutions (only a few—but very important—points are of lower resolution), the overall loss of spatial resolution is difficult to quantify. The correction data, which lie at the center of *k*-space and therefore determine the intensity of broad (low spatial frequency) regions, are less well resolved. The remainder of the data (which describe higher spatial frequencies) tend to define edges of regions, and are better resolved. If the images are used to evaluate the total matrix content, this is a perfectly reasonable situation. If, however, the images are used to spatially map the location of matrix in microscopic detail, the compromise in spatial resolution may be more significant, and a more intense gradient in the second acquisition will be necessary.

The overall resolution of WASPI is limited by Δx_p whenever the projection gradient is large enough to reduce Δx_i to relative insignificance. There are several ways to improve Δx_p. One is to increase the number of data samples per projection used in the reconstruction (N_{PS}). This will increase the maximum value mapped in *k*-space, k_{max}, without changing other parameters, resulting in a smaller Δx_p, since in principle, $\Delta x_p \sim 1/(2k_{max})$. However, there are two prominent factors that limit the maximum value of N_{PS}: The first factor is the short proton T_2* of the solid bone matrix (well after T_2*, only noise is sampled). The second factor is that as more data samples are used in each projection, the distance in *k*-space between data samples in adjacent projections becomes wider at high spatial frequencies. It should be noted that this distance must be compatible with the distance between adjacent data points within a projection ray, or *k*-space will be undersampled at the periphery. To avoid these problems, the second method to improve Δx_p is to increase *P*, which will increase the number of independent pixels (N_{IP}), and hence reduce Δx_p. The disadvantage of this method is that it requires longer scanning times, since otherwise the SNR will be adversely affected. Therefore, the balance between resolution and SNR must be considered.

In the case of measuring the degree of mineralization, several bone biopsy studies have pointed out that to accurately diagnose defects in mineralization, it is very important to use the mean values measured over many osteoid (organic matrix) seams and over multiple stages in the bone remodeling cycle, and not to use the quantities found in one individual osteoid seam and at the instantaneous stage of that osteoid seam (37). Until now, such measurements could only be made by histomorphometry of biopsy specimens. Therefore, the sampling could only be spatially sparse and limited to a very few sites in the body (e.g., the iliac crest) that are surgically accessible and not likely to introduce serious risk of weakening a load-bearing bone. In light of this observation, the 0.4-mm resolution should be adequate for accurately characterizing bone matrix density in rat bone specimens. It is important to recognize that it is unnecessary to spatially resolve individual trabeculae when making this measurement, because broad spatial averages are in fact desirable.

In this study the SNR was ~50 in cortical bone and ~10 in trabecular bone. The signal intensity of cortical bone was generally five times higher than that of trabecular bone in WASPI images (Fig. 10). The bone specimens were from healthy rats, and the BMD and the bone matrix density should be proportional, assuming a fixed degree of mineralization. The ratio of proton signal intensity of cortical bone over trabecular bone observed in this study is consistent with our earlier ^{31}P SMRI study of BMD (13).

We optimized the SNR by using the Ernst angle. In this process it is important to measure the proton T_1 of the solid bone matrix and the exact excitation angle within bone tissues. Since the proton T_2* of solid bone matrix is short and often comparable to the length of a π pulse, it is not feasible to apply an inversion recovery pulse sequence to measure T_1 in most cases. Instead, a progressive-saturation sequence is used to measure T_1. If the excitation angle

is exactly 90°, the data can be fitted to a simple exponential model:

$$M = A\{1 - \exp(-\mathrm{TR}/T_1)\}. \quad [15]$$

When the excitation angle is much smaller than 90°, as is the case for these SMRI measurements, the more precise expression for the magnetization (Eq. [14]) should be used. If a standard three-parameter exponential formula

$$M = A\{1 - B\exp(-\mathrm{TR}/T_1)\}, \quad [16]$$

is used, a deceptively satisfactory (i.e., low chi-squared) curve fit can be obtained, but the fitted parameters may be in error. For the same data reported in the Results section, Eq. [14] resulted in $T_1 = 3.7$ s and excitation angle $\beta = 16°$ (90° pulse duration = 45 μs), while Eq. [16] resulted in $T_1 = 0.45$ s and $B = 0.68$ (Fig. 8b). The exact physical meaning of B in Eq. [16] is ambiguous. We therefore recommend using Eq. [14] rather than the standard three-parameter formula (Eq. [16]) to achieve reliable results.

The achievable SNR in a given scanning time can be expressed as:

$$\mathrm{SNR} \sim (1/\mathrm{TR})^{1/2}\{1 - \exp(-\mathrm{TR}/T_1)\} \times(\sin\beta)/\{1 - (\cos\beta)\exp(-\mathrm{TR}/T_1)\}. \quad [17]$$

Equation [17] shows that for a fixed scanning time T, SNR is a very smooth function of TR between 100 ms and 200 ms with $T_1 = 3.7$ s and $\beta = 16°$, provided that the FID is averaged over N scans, where $N = T/(\mathrm{TR} \times P)$. In this study we chose TR = 150 ms.

The other issue related to the SNR and signal homogeneity is the excitation RF pulse length. As shown in Fig. 2, although a 5-μs (10°) rectangular pulse excites rather uniformly across the 200-kHz frequency range, which is the default W_S in this study, the signal intensity is much weaker than that obtained with the 8 μs pulse (16°). The MR signal response to an 8-μs excitation pulse shows a less uniform excitation profile but stronger signal. Considering that most of the regions of interest (ROIs) are within 75% of the FOV, and signal calibration (compensating for the B_1-field excitation profile) will be performed in quantitative image processing, we chose the 8-μs rectangular pulse to provide a better SNR.

One could further improve the SNR by optimizing the MR probe, striking a balance between the signal sensitivity and the RF field homogeneity. RF homogeneity is always a major concern in proton density MRI, and it is even more so when WS and FS pulses are utilized in WASPI experiments. In this study we improved the RF field homogeneity by applying a split solenoid design (two solenoid coils instead of one long solenoid). Nevertheless, it would be desirable to improve the sensitivity even further without compromising RF field homogeneity. According to the reciprocity theorem, the sensitivity can be measured by the strength of the B_1 field, expressed as the length of a 90° pulse. In this study, the 90° pulse at the center of the sample was about 50 μs. This probe was originally designed as a dual resonant $^1H/^{31}P$ RF probe, and component values were based on simulations of the losses in the circuit in order to maximize ^{31}P sensitivity (for bone mineral studies) with only a slight degradation for ^1H. If we could shorten the proton 90° pulse applied with the same power to 25 μs by limiting the power loss, we could significantly enhance the probe sensitivity and the overall SNR.

It is very important to suppress bone marrow as a whole in bone tissues to obtain the true measurement of the density of the solid bone matrix. In our original study (15) we used an on/off π pulse to further suppress the signal from bone marrow by canceling residual z-magnetization on alternate scans. In this study we found that suppression with a selective π pulse is better than that with no π pulse (depending on only the dephasing caused by the single π/2 pulse). However, in practice a number of factors can prevent the π pulse from acting ideally, such as an incorrectly set amplitude or a bandwidth that is set either too small or too large. We found empirically that substituting a second selective π/2 pulse for the selective π pulse improves the water and fat suppression even more, possibly because a π/2 pulse is partially self-compensating and may perturb the solid-state signal less.

The use of the chicken bone marrow phantom imaged with bone specimens enabled us to calibrate the degree of water and fat suppression in the WASPI images. However, the presence of the phantom affects the shimming, and the phantom may reside at a different local B_0 field, often resulting in a shift between the water peaks in rat bone and chicken marrow, as shown in Fig. 9. The marrow of rat bone contains little fat, as reported in the literature, particularly in young rats. The fat peak of the rat bone marrow is not visible in Fig. 9. It would be better to use an internal suppression reference, such as a region within the rat bone medullary cavity, where there is only bone marrow and no solid bone substance. However, such ideal marrow-only regions are hard to find in the medullary cavity within the 12-mm FOV of the distal femur, based on the observation that trabecular bone exists in the medullary cavity in the μCT images of the same rat distal femur (150 μm resolution and FOV of 1.2 mm) (Fig. 10). A more rigorous shimming improved the B_0 homogeneity and reduced the shift between the water peaks of rat bone and chicken marrow, and made the suppression more complete (Fig. 12).

The correlation between the dark regions in the NS SMRI images and the bright regions in the WASPI and μCT images of the rat bone specimens justifies the conclusion that these regions represent solid bone matrix. Collagen, the major component in the organic matrix of bone substance, is a highly ordered, motionally restricted, fibrous structural protein that exhibits a huge number of unresolved proton resonances with T_2^* values ranging down to tens of microseconds. The shortest T_2^* resonances are not correctly described by the Bloch equations (which are phenomenological and do not correctly predict the behavior of coupled spins), but rather behave as strictly solid-state spin systems. There is substantial evidence from multinuclear solid-state spectroscopy that some collagen side chains exhibit significant degrees of molecular motion and yield relatively narrow resonances even in mineralized tissue (38). It is only the longer T_2^* resonances associated with the solid matrix, with spectral linewidths on the order of 1 kHz, that contribute significantly to the

WASPI images, because the shorter T_2* signals are not spatially resolved and contribute only broad background intensity. Therefore, we detect in the WASPI images only a fraction of the signal contributed by protons on collagen molecules. The other source of the observed proton signal comes from exchangeable protons on collagen, from water strongly associated with collagen (this water exhibits a much broader linewidth compared to free water), and from motionally restricted free matrix water (which also has a broad linewidth). The term "solid bone matrix signal" in this paper refers to signal from all of these sources. However, one can translate the signal intensity measurement from WASPI into a true bone matrix density measurement by calibrating the solid bone matrix signal against a phantom constructed with several compartments of various densities of dry bovine tendon powder diluted with a nonreactive, proton-free material, such as clean, dry quartz sand. As long as a good correlation between the calibrated WASPI image intensity under defined instrumental conditions and the matrix content determined by a suitable chemical analysis can be achieved, a measurement of true matrix density can be achieved by WASPI.

The WASPI and μCT images shown in Fig. 10 were selected because of their visual similarity, and no attempt at precise image registration was made in this study. To calculate the degree of bone mineralization, coregistration methods, such as a calculus-based minimization procedure (39), would be needed to align WASPI and μCT images.

CONCLUSIONS

This study demonstrates that visualizing the solid matrix of rat bone by WASPI with a 0.4-mm resolution is feasible. One can correct the image artifacts caused by losing data points in the receiver dead time by including additional data acquired with a lower projection gradient strength, which approximately recovers the missing data. Proton solid-bone-matrix-only MR images of rat femur bone specimens were obtained for the first time. This method provides a noninvasive means of measuring bone matrix density in small animals, and should be applicable to humans when implemented on clinical scanners.

By combining WASPI measurements with CT or ^{31}P SMRI measurements of BMD, one will be able to determine the degree of bone mineralization in rat bone. We envision that this new approach will enable more-complete bone scans than can be accomplished with existing methodologies. Such a complete bone scan would yield more information than routine DXA or CT can provide, since it would characterize the bone "quality" in addition to quantity (usually considered equivalent to bone mineral content). The mineral density could be imaged by DXA or CT as appropriate (considering the cost, body part, and radiation exposure), or might also be imaged with ^{31}P SMRI. Detailed 3D bone geometry and microarchitecture could be obtained with CT or high-resolution conventional MRI, and matrix density could be imaged by WASPI, yielding the degree of mineralization when combined with the other image data.

REFERENCES

1. Parfitt AM. Bone quality: definition, history, current overview. In: NIAMS/ASBMR/NIBIB/INSERM Joint Conference on Bone Quality: What Is It and Can We Measure It? Bethesda, MD USA, May 2–3, 2005.
2. Klibanski A, et al. NIH consensus development panel on osteoporosis prevention, diagnosis, and therapy. JAMA 2001;285:785–795.
3. Evans GP, Behiri JC, Currey JD, Bonfield W. Microhardness and Young's modulus in cortical bone exhibiting a wide range of mineral volume fraction, and in a bone analogue. J Mater Sci Mater Med 1990; 1:38–43.
4. Meunier PJ, Boivin G. Bone mineral density reflects bone mass but also the degree of mineralization of bone: therapeutic implications. Bone 1997;21:373–377.
5. Mann S, Weiner S. Biomineralization: structural questions at all length scales. J Struct Biol 1999;126:179–181.
6. Parfitt AM, Qiu S, Rao D.S. The mineralization index—a new approach to the histomorphometric appraisal of osteomalacia. Bone 2004;35: 320–325.
7. Monier-Faugere M-C, Langub MC, Malluche HH. Bone biopsies: a modern approach. In: Avioli LV, Drane SM, editors. Metabolic bone disease and clinically related disorders. 3rd ed. San Diego: Academic Press; 1998. p 237.
8. Glimcher MJ. The nature of the mineral phase in bone: biological and clinical implications. In: Avioli LV, Krane SM, editors. Metabolic bone disease and clinically related disorders. New York: Academic Press; 1997. p 23–50.
9. Riggs BL, Melton LJ. Bone turnover matters: the raloxifene treatment paradox of dramatic decreases in vertebral fractures without commensurate increases in bone density. J Bone Miner Res 2002;17:11–14.
10. Borah B, Dufresne TE, Cockman MD, Gross GJ, Sod EW, Myers WR, Combs KS, Higgins RE, Pierce SA, Stevens ML. Evaluation of changes in trabecular bone architecture and mechanical properties of minipig vertebrae by three-dimensional magnetic resonance microimaging and finite element modeling. J Bone Miner Res 2000;15:1786–1797.
11. Krug R, Banerjee S, Han ET, Newitt DC, Link TM, Majumdar S. Feasibility of in vivo structural analysis of high-resolution magnetic resonance images of the proximal femur. Osteoporos Int 2005;16:1307–1314.
12. Gomberg BR, Wehrli FW, Vasilic B, Weening RH, Saha PK, Song HK, Wright AC. Reproducibility and error sources of micro-MRI-based trabecular bone structural parameters of the distal radius and tibia. Bone 2004;35:266–276.
13. Wu Y, Ackerman JL, Chesler DA, Li J, Neer RM, Wang J, Glimcher MJ. Evaluation of bone mineral density using three dimensional solid state phosphorus-31 NMR projection imaging. Calcif Tissue Int 1998;62: 512–518.
14. Wu Y, Chesler DA, Glimcher ML, Garrido L, Wang J, Jiang HJ, Ackerman JL. Multinuclear solid state three dimensional MRI of bone and synthetic calcium phosphates. Proc Nat Acad Sci USA 1999;96:1574–1578.
15. Wu Y, Ackerman JL, Chesler DA, Graham L, Wang Y, Glimcher MJ. Density of organic matrix of native mineralized bone measured by water and fat suppressed proton projection MRI. Magn Reson Med 2003;50:59–68.
16. Wu Y, Ackerman JL, Chesler DA, Wang J, Glimcher MJ. In vivo solid state ^{31}P MRI of human tibia at 1.5 T. In: Proceedings of the 7th Annual Meeting of ISMRM, Philadelphia, PA, USA, 1999 (Abstract 313).
17. Robson MD, Gatehouse PD, Bydder GM, Neubauer S. Human imaging of phosphorus in cortical and trabecular bone in vivo. Magn Reson Med 2004;51:888–892.
18. Reichert IL, Robson MD, Gatehouse PD, He T, Chappell KE, Holmes J, Girgis S, Bydder GM. Magnetic resonance imaging of cortical bone with ultrashort TE pulse sequences. Magn Reson Imaging 2005;23:611–618.
19. Glover GH, Pauly JM, Bradshaw KM. Boron-11 imaging with a three-dimensional reconstruction method. J Magn Imaging 1992;2:47–52.
20. Anumula S, Magland J, Wehrli SL, Zhang H, Ong H, Song HK, Wehrli FW. Measurement of phosphorus content in normal and osteomalacic rabbit bone by solid-state 3D radial imaging. Magn Reson Med 2006; 56:946–952.
21. Pauly JM, Conolly SM, Macovski A. Suppression of long-T_2 components for short-T_2 imaging. In: Proceedings of the 10th Annual Meeting of SMRI, New York, NY, USA, 1992 (Abstract 330).
22. Fernández-Seara MA, Wehrli SL, Wehrli FW. Multipoint mapping for imaging of semi-solid materials. J Magn Reson 2003;160:144–150.

23. Fernández-Seara MA, Wehrli SL, Takahashi M, Wehrli FW. Water content measured by proton-deuteron exchange NMR predicts bone mineral density and mechanical properties. J Bone Miner Res 2004;19: 289–296.
24. Mastikhin IV, Balcom BJ, Shah NJ. Slice selective imaging of short T_2* rigid biological tissues. In: Proceedings of the 7th Annual Meeting of ISMRM, Philadelphia, PA, USA, 1999 (Abstract 265).
25. Halse M, Rioux J, Romanzetti S, Kaffanke J, MacMillan B, Mastikhin I, Shah NJ, Aubanel E, Balcom BJ. Centric scan SPRITE magnetic resonance imaging: optimization of SNR, resolution, and relaxation time mapping. J Magn Reson 2004;169:102–117.
26. Feldkamp LA, Goldstein SA, Parfitt AM, Jesion G, Kleerekoper M. The direct examination of three-dimensional bone architecture in vitro by computed tomography. J Bone Miner Res 1989; 4:3–11.
27. Kinney JH, Lane NE, Haupt DL. In vivo, three dimensional microscopy of trabecular bone. J Bone Miner Res 1995;10:264–270.
28. Ruegsegger P, Koller B, Muller R. A microtomographic system for the nondestructive evaluation of bone architecture. Calcif Tissue Int 1996; 58:24–29.
29. Lotinun S, Evans GL, Bronk JT, Bolander ME, Wronski TJ, Ritman EL, Turner RT. Continuous parathyroid hormone induces cortical porosity in the rat: effects on bone turnover and mechanical properties. J Bone Miner Res 2004;19:1165–1171.
30. Liang Z-P, Lauterbur PC. Principles of magnetic resonance imaging. New York: IEEE Press; 2000. 91 p.
31. Slichter CP. Principles of magnetic resonance. Berlin: Springer-Verlag; 1996. 655 p.
32. Chesler DA, Vevea JM, Boada FE, Reese T, Chang C, Barrére BJ, Liu AM, Thulborn KR. Rapid 3-D reconstruction from 1-D projections for metabolic MR imaging of short T_2 species. In: Proceedings of the 11th Annual Meeting of SMRM, Berlin, Germany, 1992 (Abstract 665).
33. Kuethe DO, Caprihan A, Lowe IJ, Madio DP, Gach HM. Transforming NMR data despite missing points. J Magn Reson 1999;139:18–25.
34. Chesler DA. Reducing dead time effect in MRI projection. U.S. patent 6,879,156; 2005.
35. Ernst RR, Bodenhausen G, Wokaun A. Principles of nuclear magnetic resonance in one and two dimensions. Oxford: Clarendon Press; 1987. p 124.
36. Morris PG. Nuclear magnetic resonance imaging in medicine and biology. Oxford: Clarendon Press; 1986. p 51.
37. Parfitt AM. Osteomalacia and related disorders. In: Avioli LV, Drane SM, editor. Metabolic bone disease and clinically related disorders. 3rd ed. San Diego: Academic Press; 1998. p 328.
38. Sarkar SK, Hiyama Y, Niu CH, Young PE, Gerig JT, Torchia DA. Molecular dynamics of collagen side chains in hard and soft tissues. A multinuclear magnetic resonance study. Biochemistry 1987;26:6793–6800.
39. Woods RP, Grafton ST, Holmes CJ, Cherry SR, Mazziotta JC. Automated image registration: I. General methods and intrasubject, intramodality validation. J Comput Assist Tomogr 1998;22:139–152.